Closed-loop Characterization of Noise and Stability in a Mode-localized Resonant MEMS Sensor

Milind Pandit, *Student Member, IEEE,* Chun Zhao, Guillermo Sobreviela, Arif Mustafazade, Sijun Du, *Student Member, IEEE,* Xudong Zou, *Member, IEEE,* and Ashwin. A. Seshia, *Senior Member, IEEE*

***Abstract*—This paper presents results from the closed-loop characterization of an electrically coupled mode-localized sensor topology including measurements of amplitude ratios over long duration, stability, noise floor and the bandwidth of operation. The sensitivity of the prototype sensor is estimated to be -5250 in the linear operation regime. An input-referred stability of 84ppb with respect to normalized stiffness perturbations is achieved at 500s. When compared to frequency shift sensing within the same device, amplitude ratio sensing provides higher resolution for long term measurements due to the intrinsic common mode rejection properties of a mode-localized system. A theoretical framework is established to quantify noise floor associated with measurements validated through numerical simulations and experimental data. In addition, the operating bandwidth of the sensor is found to be 3.5Hz for 3dB flatness.**

***Index Terms*—MEMS, force sensor, resonant sensor, force sensitivity, thermal noise**

I. Introduction

ENABLING technologies such as vacuum encapsulation [2] have accelerated the development of MEMS resonators in the past decade. Due to its intrinsic advantage of high stability, MEMS resonators have been employed as accurate timing references [3], [4], filters [5], [6], and various sensors including but not limited to accelerometers [7]–[10], magnetometers, [11], [12], temperature [13] and pressure sensors [14].

Due to the quasi-digital nature, conventionally MEMS resonant sensors have used resonant frequency shifts as an output metric. However, limited by the slow drifts and random walk [15], the frequency instability of MEMS resonators can affect the long-term measurement accuracies. The conventional solutions to this problem include temperature compensation [16], [17], and differential cancellation specifically for sensing applications [18], [19]. However, there are issues with these solutions: the temperature compensation electronics typically consumes more power than the oscillator electronics, which is less suitable for low power applications; whereas differential cancellation becomes less effective in the presence of mismatch between the resonators [20].

This is an extended version of a conference paper presented at 2017 European Frequency and Time Forum & International Frequency Control Symposium [1].

M. Pandit, C. Zhao, G. Sobreviela, A. Mustafazade, Sijun Du and A. A. Seshia are with the Nanoscience centre, University of Cambridge, Cambridge, CB3 0FF, UK. E-mail: mnp26@cam.ac.uk (M. Pandit), cz319@cam.ac.uk (C. Zhao), aas41@cam.ac.uk (A. A. Seshia)

X. Zou is with the Institute of Electronics, Chinese Academy of Sciences, Beijing 100190, China.

M. Pandit and C. Zhao are equally contributing principle authors

Manuscript sent September 30, 2017.

Recently, a new sensing paradigm, termed as mode-localized sensing [21], [22], has been proposed with an enhanced common mode rejection capability [23], [24]. This type of sensor is based on the principle of vibration mode-localization [25], where the modal amplitude pattern, e.g. amplitude ratio or difference [26], changes when the system is subject to an external perturbation. The perturbation can be an inertial force [27], electrostatic force [28], [29] or a mass change [30]. Despite the potential relative disadvantage associated with amplitude readout [31], an elevated sensitivity, i.e. up to four orders of magnitude [32], compared to conventional resonant sensors with frequency shift output, has enabled these sensors to achieve an improved input-referred stability. This is particularly the case for long duration measurements, where the amplitude noise can be reduced by averaging assuming white noise characteristics.

In this paper, experimental results validating the claim of amplitude ratio stability, particularly over long integration times are presented. The prototype mode-localized MEMS resonant sensor used in the experiment is driven using a closed-loop configuration. The experimental setup represents an advancement over the closed-loop configuration previously reported in [33]. For the first time, the bandwidth associated with the amplitude ratio measurements in such a configuration is presented. The amplitude ratio stability is then compared to the frequency stability. With the sensitivity of amplitude ratio and frequency shift as output metrics, the input-referred stability for each sensing approach is consequently compared. The theoretical prediction of noise in amplitude ratio measurements in a 2-DOF mode localized system is presented, and is validated by comparison between simulated and experimental data.

II. Theory

A. Linear Dynamics

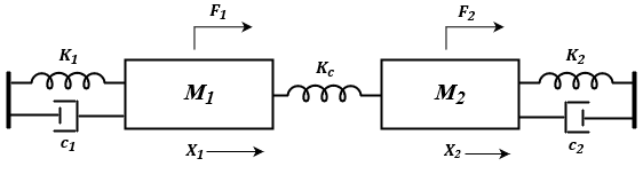

Fig. 1. Spring-mass-damper schematic of a 2-DOF coupled resonator system.

The linear dynamics of a two-degree-of-freedom (2-DOF) weakly coupled resonator system is schematically expressed

in Fig. 1. Using the figure, following equations of motion can be derived:

$$M_1\ddot{X}_1 + c_1\dot{X}_1 + K_1X_1 + K_c(X_1 - X_2) = F_1 \tag{1a}$$

$$M_2\ddot{X}_2 + c_2\dot{X}_2 + K_2X_2 + K_c(X_2 - X_1) = F_2 \tag{1b}$$

Where M_r, c_r, K_r, F_r and $X_r (r = 1, 2)$ denote the mass, damping, stiffness, actuation force applied and displacement of the rth resonator. Using the transfer function based model described in [32], the expressions for displacement of *r*th resonator with respect to a force on the *j*th resonator is derived in detail in Appendix A. The results of the derivation show that:

$$X_r = \sum_{j=1}^{2} H_{rj}F_j \tag{2}$$

The transfer functions (H_{rj}) for various inputs and outputs can be described as follows:

$$H_{11} = \frac{H_2(s)}{H_1(s)H_2(s) - K_c^2}; H_{12} = \frac{K_c}{H_1(s)H_2(s) - K_c^2}; \tag{3a}$$

$$H_{21} = \frac{K_c}{H_1(s)H_2(s) - K_c^2}; H_{22} = \frac{H_1(s)}{H_1(s)H_2(s) - K_c^2}; \tag{3b}$$

where the individual transfer functions H_1 and H_2 are given by the expressions:

$$H_1(s) = M_1s^2 + c_1s + K_1 + K_c \tag{4a}$$

$$H_2(s) = M_2s^2 + c_2s + K_2 + K_c \tag{4b}$$

Here, the typical configuration of a mode-localized MEMS resonant sensor with identical parameters is considered, i.e. $M_1 = M_2 = M, c_1 = c_2 = c$, $K_1 = K$ and $K_2 = K + \Delta K$, where $\Delta K \ll K$ is the stiffness perturbation applied on resonator 2. Assuming the system is only driven from one side, i.e. $F_1 = F$ and $F_2 = 0$, the transfer functions in Eqs. 3a and 3b can be simplified to:

$$X_1 = \frac{H_2(s)}{H_1(s)H_2(s) - K_c^2}F \tag{5a}$$

$$X_2 = \frac{K_c}{H_1(s)H_2(s) - K_c^2}F \tag{5b}$$

The modal frequencies and the amplitude ratio at each mode can be expressed as:

$$\omega_1^2 = \frac{2K - \Delta K - \sqrt{(\Delta K)^2 + 4K_c^2}}{2M}; \tag{6a}$$

$$\left|\frac{X_1}{X_2}\right|_{\omega_1} = \frac{\Delta K - \sqrt{(\Delta K)^2 + 4K_c^2}}{2K_c}; \tag{6b}$$

$$\omega_2^2 = \frac{2K - \Delta K + \sqrt{(\Delta K)^2 + 4K_c^2}}{2M}; \tag{6c}$$

$$\left|\frac{X_1}{X_2}\right|_{\omega_2} = \frac{\Delta K + \sqrt{(\Delta K)^2 + 4K_c^2}}{2K_c} \tag{6d}$$

B. Amplitude Noise

The amplitude noise in the system can be attributed to thermal noise from the mechanical resonators and electrical noise from the amplifier circuit. In this section, these two noise sources are modeled and their impact on the resolution of the amplitude ratio measurements are discussed.

1) Thermal Noise: The thermal noise originates from the intrinsic Brownian motion of the particles of mass in the resonators. Using the transfer function approach as outlined in Appendix A, the noise power of the amplitude noise can be modeled (assuming that the thermal noise is a driving force) as [34]:

$$\langle T_{Xr}(\omega)\rangle^2 = \sum_{j=1}^{2} \mid H_{rj}(\omega)F_{n,j}(\omega) \mid^2 \tag{7}$$

Where $H_{rj}(\omega)$ is the transfer function of the system from the *j*th input to the *r*th output and the power spectral density of the thermal noise is given by [35]:

$$F_{n,j}(\omega)^2 = \frac{1}{2\pi}4K_BTc_r\Delta\omega \tag{8}$$

Where K_B is the Botlzmann's constant, T is the ambient temperature of operation and c_r is the damping constant of the *r*th resonator. Note here that in all the future calculations, the angular frequency is used so the power spectral density with respect to the customary 1Hz bandwidth is converted into the equivalent angular frequency.

Using the transfer functions as described in Eq. 3a and 3b, the various contributions to a thermal noise forcing stated in Eq. 8 for each mode can be found to be:

$$\langle T_{X1}(\omega)\rangle^2 = \mid H_{11}(\omega) \mid^2 F_{n,1}(\omega)^2 + \mid H_{12}(\omega) \mid^2 F_{n,2}(\omega)^2 \tag{9a}$$

$$\langle T_{X2}(\omega)\rangle^2 = \mid H_{21}(\omega) \mid^2 F_{n,1}(\omega)^2 + \mid H_{22}(\omega) \mid^2 F_{n,2}(\omega)^2 \tag{9b}$$

The amplitude noise calculated is then converted into sense noise current using the transduction factor:

$$\langle i_{Tr}(\omega)\rangle = V_{DC}\frac{\epsilon_0 A_e}{d^2}\omega \langle T_{Xr}(\omega)\rangle; \quad r = 1, 2; \tag{10}$$

Based on these equations, the thermal noise in both the resonators is calculated in the operating region (biased away from veering zone) and a representative response is plotted in Fig. 2.

2) Electrical noise: The electrical noise is dominated by the first stage transimpedance amplifier (TIA), which converts with motional current from the MEMS resonator to voltage. An ultra-low-noise two-stage transimpedance amplifier structure (as shown in Fig. 3) is used [36]. A bias-T consisting of R_b and C_{bias1} are used to DC bias the sense electrode of the MEMS resonator (MEMS input port in Fig. 3). R_f and C_f provide the feedback network for the first stage charge amplifier with U_1. $C_{p,d}$ and $C_{p,u1}$ are the parasitic capacitance of the device and the op amp U_1, respectively. A second-stage differentiator consists of C_d, R_d and U_2, ensuring a flat gain and phase response in the frequency band while providing

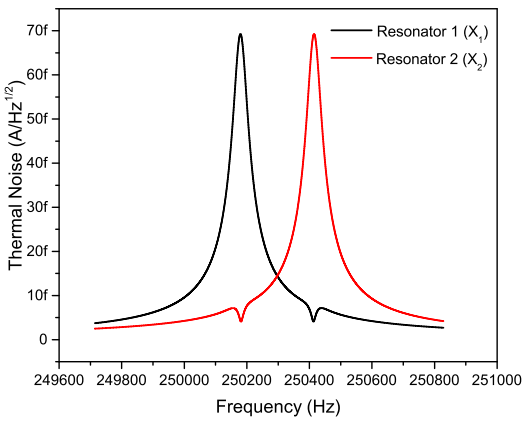

Fig. 2. Thermal noise in both resonators simulated across the frequency of interest.

a gain boost. Since the input parasitic capacitance of $U2$ is generally much smaller than C_d, it is therefore neglected.

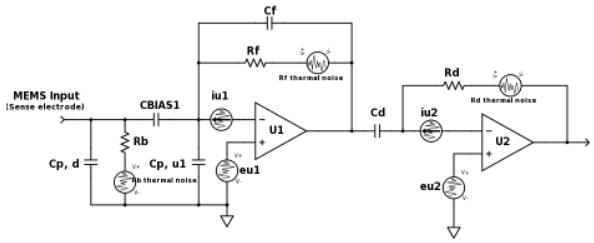

Fig. 3. A two-stage transimpedance amplifier topology, with the main noise sources included schematically.

The noise current at the input node, i_n, can be expressed by [37]:

$$\begin{aligned}\bar{i}_n(f)^2 = &(\bar{i}_{u1})^2 + (\bar{e}_{u1})^2\left[2\pi f(C_f + C_{p,d} + C_{p,u1})\right]^2 \\ &+ (\bar{e}_{u1})^2\left[\left(\frac{1}{R_b}\right)^2 + \left(\frac{1}{R_f}\right)^2\right] \\ &+ \left[\left(\frac{C_f}{C_d}\right)^2 + \left(\frac{1}{2\pi f R_f C_d}\right)^2\right] \\ &\times \left[(\bar{i}_{u2})^2 + (\bar{e}_{u2})^2(2\pi f C_d)^2 + \left(\frac{\bar{e}_{u2}}{R_d}\right)^2 + \frac{4kT}{R_d}\right] \\ &+ \frac{4kT}{R_b} + 4kTR_f\left[\left(\frac{1}{R_f}\right)^2 + (2\pi f C_f)^2\right]\end{aligned} \tag{11}$$

It should be pointed out that near the operating region, $1/2\pi f C_f \ll R_f$; also due to the high gain of the first stage, the noise contribution from the second stage can be negligible. Therefore, the total noise current at the input node can be approximated as:

$$\begin{aligned}\bar{i}_{En}(f)^2 \approx &(\bar{i}_{u1})^2 + (\bar{e}_{u1})^2\left[2\pi f(C_f + C_{p,d} + C_{p,u1})\right]^2 \\ &+ (\bar{e}_{u1})^2\left(\frac{1}{R_b}\right)^2 + \frac{4kT}{R_b}\end{aligned} \tag{12}$$

It can be seen that to optimize the noise current, R_b should be maximized, whereas $i_{u1}, e_{u1}, C_f, C_{p,d}$ and $C_{p,u1}$ should be minimized. However, R_b is directly proportional to the charge-up time of the circuit due to the bias-T, for a reasonable balance between the noise and the charge-up time, 1.6MΩ is chosen as the value of R_b. Input noise current, i_{u1}, input noise voltage, e_{u1} and input parasitic capacitance, $C_{p,u1}$, are the key specifications for the $U1$ op-amp; therefore, ADA4817 (Analog Devices, Inc.) is chosen for its optimal noise performance near the operating frequency of 250kHz. Assuming a device parasitic capacitance of $C_{p,d} = 10$pF, and choosing a $C_f = 0.1$pF (smallest for discrete capacitance), the estimated noise floor around $250kHz$ is estimated as 110fA.

C. Amplitude ratio noise

The noise in the individual amplitudes from both the thermal sources (from Eq. 10) and electrical (from Eq. 12) can be added in quadratures (since they are uncorrelated) to achieve the total noise in each of the resonator amplitudes as follows:

$$\langle i_r \rangle^2 = \langle i_{En} \rangle^2 + \langle i_{Tr} \rangle^2; \quad r = 1, 2 \tag{13}$$

The simulation and the analytical expressions show that the electrical noise in each of the measurement channels is higher than the thermal noise from the resonators themselves. This is further verified experimentally in Section III. Since the noise in the system is dominated by electrical noise, we can assume that the noise in each resonator channel are uncorrelated. With the noise in individual channels derived, the noise in amplitude ratio readout, $\left\langle \frac{i_1}{i_2} \right\rangle$, is given by [38] [39]:

$$\left(\left\langle \frac{i_1}{i_2} \right\rangle \Big/ \frac{i_1}{i_2}\right)^2 = \left(\frac{\langle i_1 \rangle}{i_1}\right)^2 + \left(\frac{\langle i_2 \rangle}{i_2}\right)^2 \tag{14}$$

where $\langle i_1 \rangle$ and $\langle i_2 \rangle$ represent the noise in the channel representing resonator 1 and 2 respectively. In the systems where the electronics noise in the readout path dominates, the noise of each resonator can be assumed to be equal due to the typically identical readout paths, thus $\langle i_1 \rangle = \langle i_2 \rangle$. The operating region in this paper is baised away from veering region where $i_1 > i_2$. Thus, the signal-to-noise-ratio (SNR) in amplitude ratio readout can be predominantly determined by the SNR of resonator 2.

III. Experiment

A. Device Description

Two identical, electrostatically coupled double ended tuning fork (DETF) resonators are used when conducting the experiments. An optical micrograph of the device is shown in Fig. 4. The device was fabricated by MEMSCAP Inc. using SOIMUMPS, a commercial foundry process that uses silicon-on-insulator (SOI) wafers. The dimensions of the device are described in Table I.

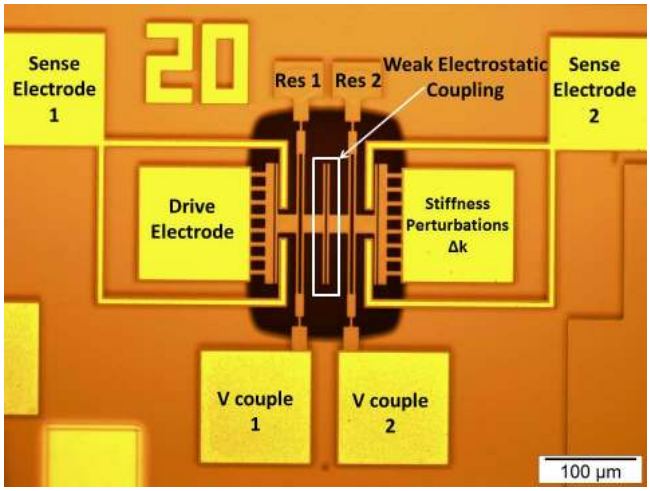

Fig. 4. Optical Micrograph of the device.

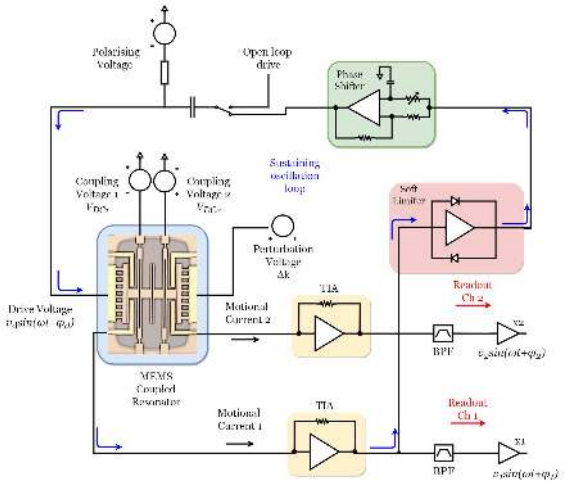

Fig. 5. Schematic of the experimental setup.

TABLE I
DEVICE PARAMETERS

Parameter	Value
Beam Length	350 μm
Beam Width	6 μm
Electrode Length	260 μm
Electrode Width	6 μm
Device Layer Thickness	25 μm
Proof Mass (2 for each DETF)	40 μm $\times$ 40 μm
Electrode Gaps	2 μm
Computed resonator stiffness (k)	1080 N/m
Computed resonator mass (m)	0.46 ng
Computed resonator natural frequency (ω_0)	245kHz
Computed coupling stiffness (k_c)	-0.46 N/m
Experimental Quality factor (k_c)	6000

B. Measurement Setup

The experimental setup is shown in Fig. 5. The two resonators are weakly coupled with negative stiffness by applying a DC voltage across the gap between the resonators. The two sense electrodes were biased at the same DC Voltage and were used to sense the vibration amplitudes (X_1 and X_2) of the resonators. A negative stiffness perturbation was applied to resonator 2 using the perturbations electrode in the form of voltage difference for sensitivity measurements.

1) Oscillator Design: The oscillator for the sensor was created using the master-slave drive configuration. The loop was closed using the output current of resonator 1 that was first converted into voltage through a Transimpedance Amplifier (TIA), then passed through a soft limiter circuit and a phase shifter to satisfy the Barkhausen criteria. Resonator 1 was driven with a combination of a DC polarizing voltage and an AC excitation voltage however, resonator 2 was only indirectly driven through the coupling. This simple oscillator topology requires the system to be biased away from the veering zone with resonator 1 having a higher amplitude of vibration that does not vary across the range of stiffness perturbations. A further advantage of working away from the veering zone is the linearity in the operating range and increased sensitivity to input perturbations in comparison to working around veering range.

IV. RESULTS AND DISCUSSION

A. Sensitivity Analysis

To achieve high sensitivity, $VDC1$ was set to 0V and $VDC2$ was set to 5V thereby applying a coupling voltage of 5V. The voltage difference for the drive and sense transductions were maintained at 35V in order to maintain equal drive and sense polarization voltages. Stiffness perturbations were applied to resonator 2 by applying a voltage to the perturbations electrode (V_p). The perturbation voltage were swept from -5V to -15V with increments of 2V. The respective values for the coupling stiffness and perturbations voltages resulting from these voltages can be calculated from the energy stored in a parallel plate capacitor and is shown in Eqns 15 and 16 .The amplitudes and frequency were first measured in open loop setup with the lock in Amplifier (MFLI, Zurich Instruments) and then in closed-loop with Digital Multimeters (34470A, Keysight) and Frequency Counters (53230A Keysight) respectively. Each measurement was averaged over a period of 1 minute. The results are plotted in Fig. 6.

$$k_c = -\frac{\epsilon_0 A_e}{d^3}(V_{DC1} - V_{DC2})^2 \tag{15}$$

$$\Delta k = -\frac{\epsilon_0 A_e}{d^3}(V_p - V_{DC2})^2 \tag{16}$$

Fig. 6 shows the sensitivity of various output variables in both open loop and closed loop configurations. Since the operation point of this sensor is away from the veering zone, the amplitude of resonator 1 stays relatively constant while that of resonator 2 increases with increased stiffness perturbations. Additionally, the observed change in amplitude ratio over stiffness perturbations is linear while the frequency shift for this mode is almost negligible due to the operating regime. The difference in the values of the open loop and closed loop measurements can be attributed to different loading conditions observed over the measuring devices. Furthermore, due to the

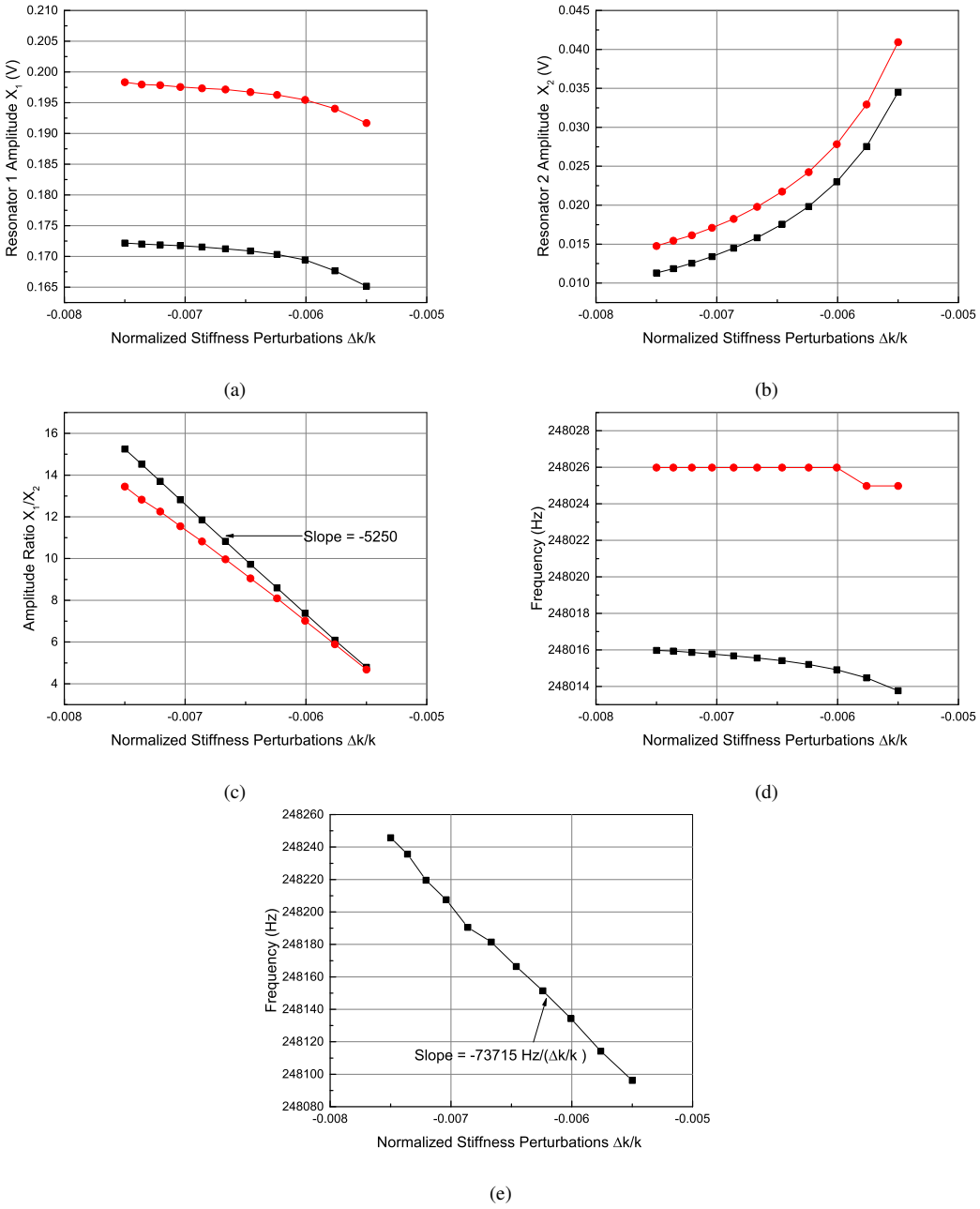

Fig. 6. Sensitivity of amplitude of resonator 1 (a) and resonator 2 (b), amplitude ratio (c), and frequency (d) in open loop (Red) and closed-loop (Black) configuration. (e) Open loop sensitivity of the resonant frequency of in-phase mode with respect to normalized stiffness perturbations.

low resolution of the open loop measurements, the frequency trend is not consistent with closed loop measurements.

The sensitivity of the amplitude ratio in terms of normalized stiffness perturbation, $\delta K = \Delta K/K$, is calculated as:

$$S_{AR} = \frac{\partial AR}{\partial(\delta K)} = -5250 \tag{17}$$

The frequency shift in this operating region is very insensitive and thus does not represent the maximum sensitivity achieved with frequency shift sensing in this device. The operating region of the oscillator is limited to the mode where the amplitude of resonator 1 is insensitive to stiffness perturbations. A byproduct of this condition with electrically coupled devices is that the frequency of the anti-phase mode (the mode being measured) remains approximately constant. This is seen in Fig. 6(d) where the closed-loop frequency changes by only 2 Hz over the range of the stiffness perturbations. In this operating region, the sensitivity of the in-phase mode is maximum. Due to the symmetry of the system, the in-phase mode stability can be assumed to be similar to the anti-phase mode stability (shown in Fig. 7). To achieve the best input-referred bias stability, the sensitivity of the in-phase mode (shown in Fig. 6e) is used for calculations of input-referred stability.

Fig. 6(e) shows the measured open loop sensitivity of the frequency shift of mode 2 in the same operation region. The slope describes the sensitivity with respect to normalized

stiffness perturbation, δK, and it is calculated as:

$$S_f = \frac{\partial f}{\partial(\delta K)} = -73715 \tag{18}$$

These sensitivity results will be further used in the calculation of the input referred stability in the stability analysis section.

B. Stability Analysis

To investigate the long term stability of the system, the sensor was placed in the closed-loop configuration with the DC perturbation voltage set to -10V while amplitude and frequency data was collected for 12 hours. The Allan deviation of the amplitude ratio and the frequency data was then calculated to indicate the stability of the two output metrics. 7a shows the absolute stability of the amplitude ratio measurements, σ_{AR}. The trend of the curve shows that the amplitude ratio output metric is more stable at higher integration times with the best stability (σ_{AR}) of 4.32×10^{-4} achieved at 500s. After 500s, the stability of amplitude ratio deteriorates with increasing integration time. One possible explanation for this can be the charge/discharge at the bias-T at the TIA. Other effects such as the stability of the voltage sources cannot be excluded. Further study is required in this aspect. In comparison, 7b shows the absolute stability of the frequency data, σ_f. In this case, the trend of the curve shows that the stability decreases with larger integration times signifying a poor long term stability. Nonetheless, a best stability (σ_f) of 0.6mHz is achieved at 0.2s integration time.

Although output stability is an important metric, the input referred stability governs the resolution of the sensor. The input referred stability in terms of normalized stiffness perturbation, $\sigma_{\delta K}$, signifies the minimum normalized perturbation that can be sensed by the mode localized system. This can be calculated for amplitude ratio and frequency as follows:

$$\sigma_{\delta K,AR} = \frac{\sigma_{AR}}{S_{AR}} \tag{19}$$

$$\sigma_{\delta K,f} = \frac{\sigma_f}{S_f} \tag{20}$$

Using the above relation, the input referred stability of both the amplitude ratio and the frequency shift are compared in 8. The trend seen in the output stability is retained in the input stability as well. Normalized perturbations δK can be resolved very well by frequency as an output metrics for shorter integration times. However, for long term measurements (in this case $\tau > 100s$), amplitude ratio measurements provide better and more stable resolution than resonant frequency measurements.

C. Noise Floor

The noise in the amplitude measurements is estimated to be from four different sources: the thermal noise of the resonators, the noise voltage from the electrical sources for the coupling and the bias voltages, the phase and amplitude noise in the oscillator, and the noise in the recording instruments (in this case, the multimeter).

The theoretical thermal noise at the resonant frequency can be calculated using Eqs. 9a, 9b and 10 and the electrical noise using Eq. 12. The two noises are shown in Table II after converting them to equivalent noise current.

TABLE II
NOISE COMPARISON

Noise Source	**Noise amplitude** $\langle i_n \rangle$
Thermal Noise	$70fA/\sqrt{\text{Hz}}$
Electrical Noise	$110fA/\sqrt{\text{Hz}}$
Total Noise (at resonance)	$156fA/\sqrt{\text{Hz}}$

To experimentally achieve the thermal noise and the noise in the voltage sources in the system, the drive signal was turned off and the noise in each of the readout channels was measured with the help of the Zurich Instruments MFLI noise analyser system. The noise in each channel is plotted in Fig. 9 in the frequency of interest. This noise includes the noise added to the measurement from voltage sources for V_{DC}, V_c and V_p.

The figure confirms the results of the theoretical calculations presented in the Theory section and Table II that the system is dominated by electrical noise from the amplifier circuit and the sources for coupling and bias voltage. The open loop response of the resonators at the operating point is also shown to confirm that there is no component of the thermo-mechanical noise in the noise response. The averaged values for noise in the two readout pathways are shown in Fig. 9 as well. There is a slight discrepancy between the two readout paths but that can be attributed such factors as non-identical cables and other experimental setup issues. The experimental calculated electrical noise can be summarized to be $140fA/\sqrt{Hz}$. The discrepancy between the theoretically estimated and measured input-referred current noise can be explained by the underestimation of the TIA feedback capacitance. In addition to the 0.1pF capacitor, parasitic capacitance in parallel would result in higher feedback capacitance, thus worsen the input-referred noise current.

The white noise floor and the corner frequency of the experimental data is estimated by extracting the noise spectral density of the long term measurement of the amplitude ratio. The NSD is plotted in Fig. 10 below along with the threshold of the electrical and thermal noise sources calculated by using the noise values shown in Fig. 9 and plugging them into Eq. 14 to calculate the amplitude ratio noise.

The amplitude ratio noise floor is seen to be at $4.4 \times 10^{-3}/\sqrt{\text{Hz}}$ but the amplitude ratio noise floor calculated using only the thermal and electrical noise sources is seen to be at $2.2 \times 10^{-3}/\sqrt{\text{Hz}}$. This means that the other two sources of noise - oscillator noise and measurement device noise, contribute to the other half of the noise that is seen in the NSD of the measurement. The corner frequency of the amplitude ratio measurements is observed at 1.7mHz which is concurrent with the long term stability observed in the Allan Deviation plot in Fig. 8.

To understand the benefits of amplitude ratio as an output metric, the input-referred NSD of both the amplitude ratio and frequency outputs are plotted in Fig. 11.

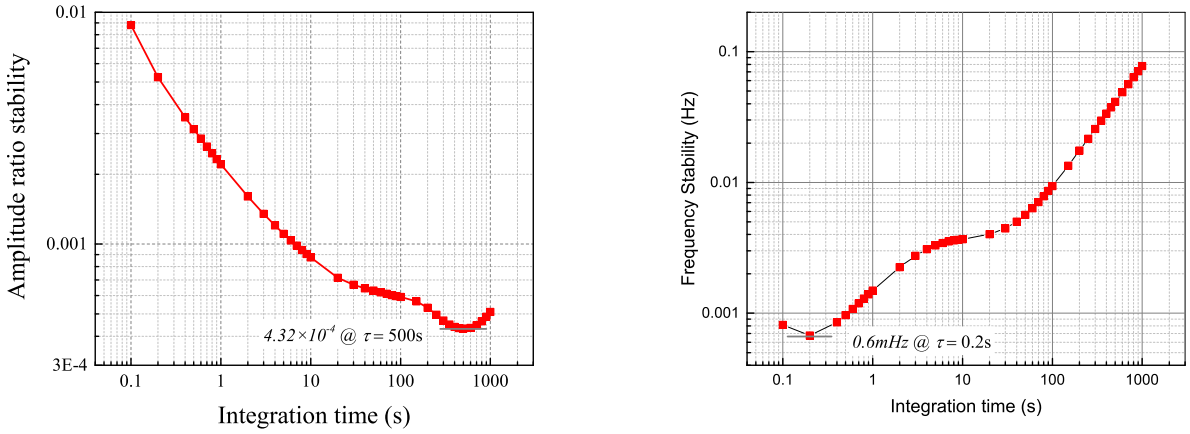

(a) (b)

Fig. 7. Figure showing the measured a) amplitude ratio and b) frequency stability. The best amplitude ratio stability of 4.32×10^{-4} occurs at $\tau = 500$s. The best frequency stability of 0.6mHz occurs at $\tau = 0.2$s. However, due to the long term drift in resonant frequency, the frequency stability worsens as the integration time increases.

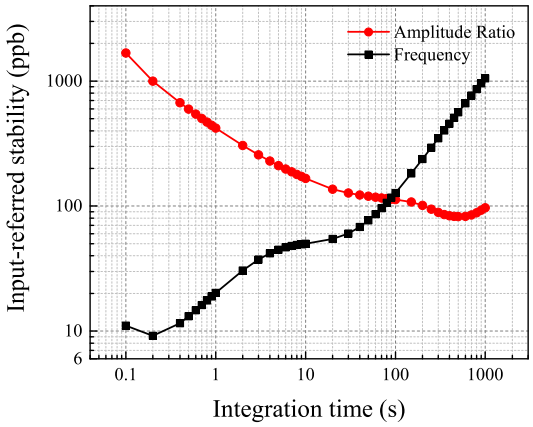

Fig. 8. Estimated input-referred stability utilizing the sensitivity values. It can be observed that the amplitude ratio achieves better stability for integration time $\tau \geq 100$s, showing the suitability of mode-localized resonant sensors employing amplitude readout for long term measurements.

It can be observed that the amplitude ratio has worse noise floor, $0.61\text{ppm}/\sqrt{\text{Hz}}$ as compared to $6\text{ppb}/\sqrt{\text{Hz}}$ for frequency noise floor. However, amplitude ratio has improved noise spectral density in the $1/f$ dependent region, for frequencies below 1mHz. This improvement can be associated to the common mode rejection to first order temperature and pressure changes compared to the conventional frequency shift measurements.

Further experiments were done by extracting the NSD of the long term amplitude ratio measurements at different perturbation voltages. Essentially, by changing the perturbation voltages, the amplitudes of vibration of the two resonators were changed and in turn, the amplitude ratio was changed. Fig. 12 shows the trend of variation of the noise floor of the amplitude ratio measurements with the change in the amplitude ratios.

This result is consistent with the theoretical noise estimation with the assumption that the electrical noise is dominant in the measurement setup. By decreasing the amplitude ratio, the amplitude of resonator 2 (which was limiting the noise floor) increases. Assuming that the electrical noise remains constant regardless of the amplitude of vibration of the resonators, decreasing the amplitude ratio reduces the noise in amplitude ratio as per Eq. 14. This experimental result is the first step towards optimizing the operating region for the mode localized sensors. It has been shown extensively that operating these sensors away from the veering zone (at high amplitude ratios) is beneficial towards its linear sensitivity and increasing the dynamic range [26] [27]. However, for the first time, these results show that it is advantageous (for reducing the noise floor) to operate at lower amplitude ratios, near the veering zone, if the system is dominated by electrical noise.

D. Bandwidth Characterization

The bandwidth of the mode-localized sensor in the closed-loop setup has been characterized by applying alternating perturbations. A square wave with maximum and minimum amplitudes of -5V and -10V was applied to the perturbation electrode at various frequencies. The frequency was swept from 0.1Hz to 10Hz with appropriate steps in between them. Similar to the sensitivity test, the amplitudes and the frequency were measured and recorded.

The real time response of the amplitude ratio to such perturbation is shown in Fig. 13. The two examples show the switching between the perturbation stages of -5V and -10V at 0.1Hz and 1Hz. The amplitude ratio at both these frequencies track the DC values of -5V and -10V thus showing that these frequencies are well within the bandwidth of the sensor.

Upon further increasing the frequency of perturbations, it is seen that the amplitude ratio values decrease with respect

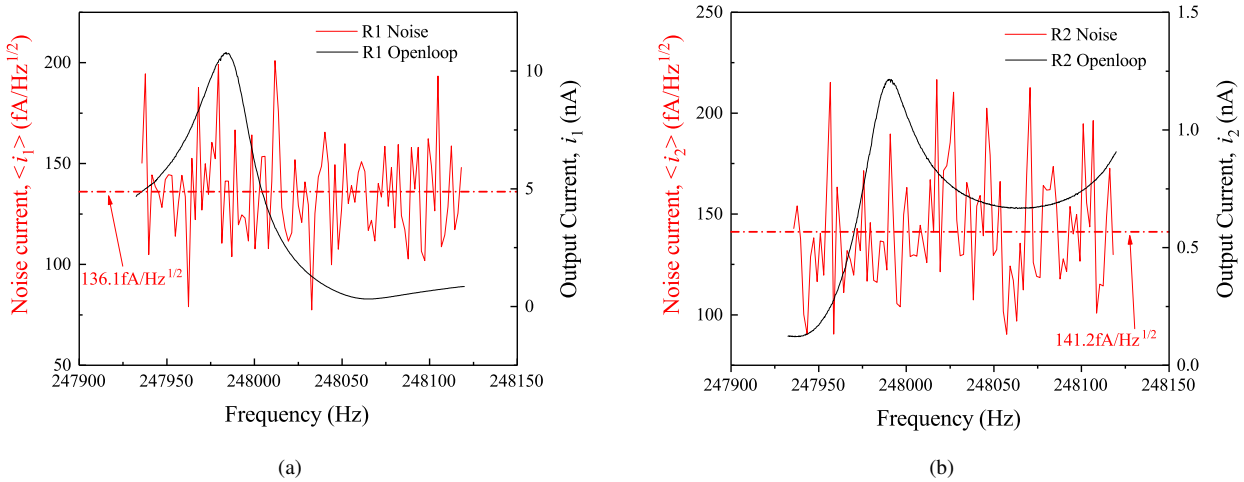

Fig. 9. Measured noise floor with the open loop response superimposed for (a) Resonator 1 and (b) Resonator 2 to show an electrical noise dominated system.

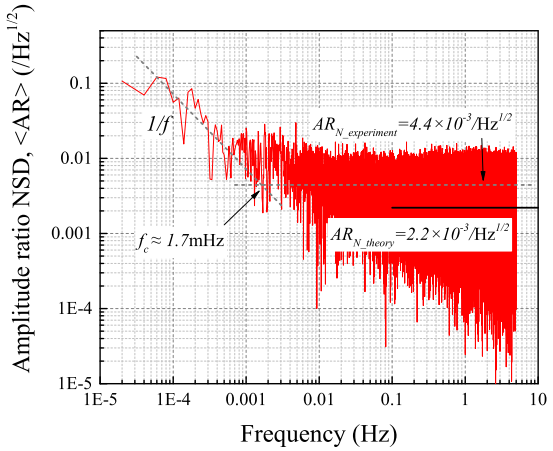

Fig. 10. Amplitude ratio noise spectral density extracted from 18-hour measurement data. It can be observed that the amplitude ratio noise spectral density is 4.4×10^{-3}. The corner frequency occurs at $f_c = 1.7$mHz.

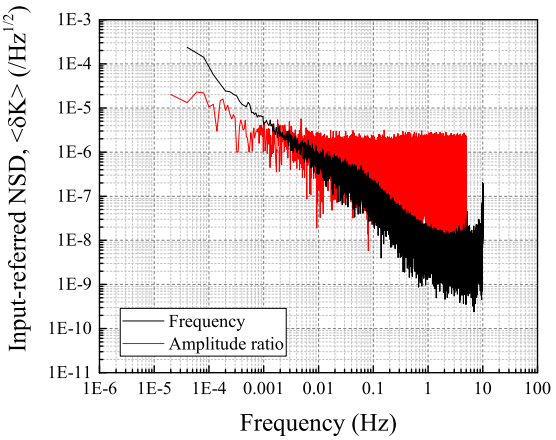

Fig. 11. Estimated input-referred noise spectral density utilizing the sensitivity values.

to the DC values seen above. To calculate the bandwidth of the sensor, the RMS value of the amplitude ratio is taken for different perturbation frequencies. This gain is normalized to the DC gain and plotted in decibels in Fig. 14. The 3dB bandwidth of the system under test as shown in the figure is 3.5Hz which is representative of the maximum frequency of perturbation that can be sensed by this system without losing information about the perturbations. Since the stiffness is modulated parametrically with time rather than a simple AM modulation of an input signal through a resonant filter, the theoretical analysis of the bandwidth is complex. This oscillator has been designed for near DC perturbation frequency and is not optimized for higher frequency perturbations but future work on oscillators for mode localized systems can result in the system working at higher frequency perturbations.

V. Conclusion and Future Work

This paper extends the work in [1] by presenting a modeling framework to study noise and resolution in a (mode localized) 2-DOF resonator system. Further results on characterizing the bandwidth of the sensor as well as observations on minimizing the noise in the amplitude ratio measurements are provided. The paper also introduces a self-sustaining oscillator topology for mode localized sensors. The advantages of using the amplitude ratio as an output metric over conventional frequency shift sensing are discussed, especially for long term measurements. A noise floor of $4.4 \times 10^{-3}/\sqrt{\text{Hz}}$ achieved is in broad agreement with the theoretical calculations. An important observation is made that the noise floor can be reduced by tuning the amplitude ratio since the measurements were dominated by noise from electrical sources.

A more detailed study of how to optimize the noise floor as well as increase the stability of the mode localized resonators

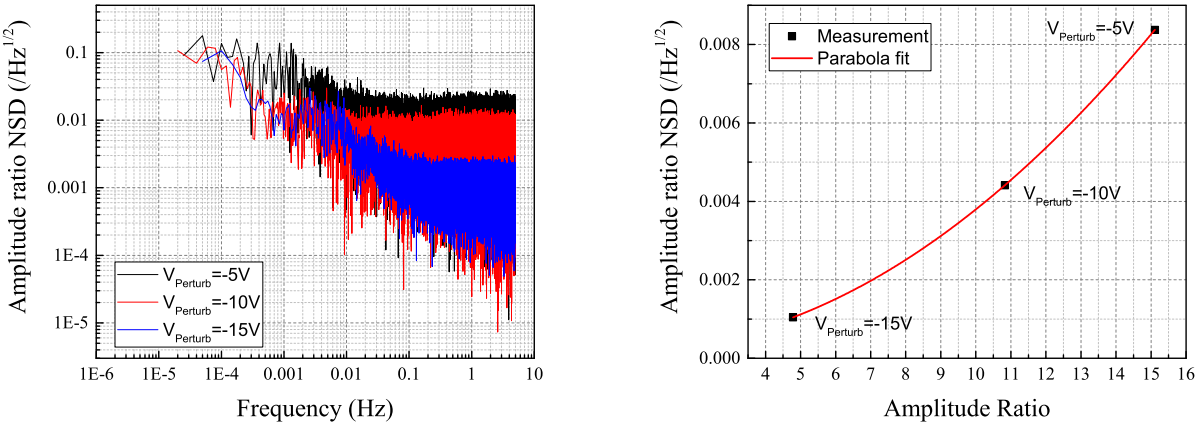

(a) (b)

Fig. 12. (a) Compares the NSD at different amplitude ratios and (b) shows that the noise floor varies parabolically with the amplitude ratio.

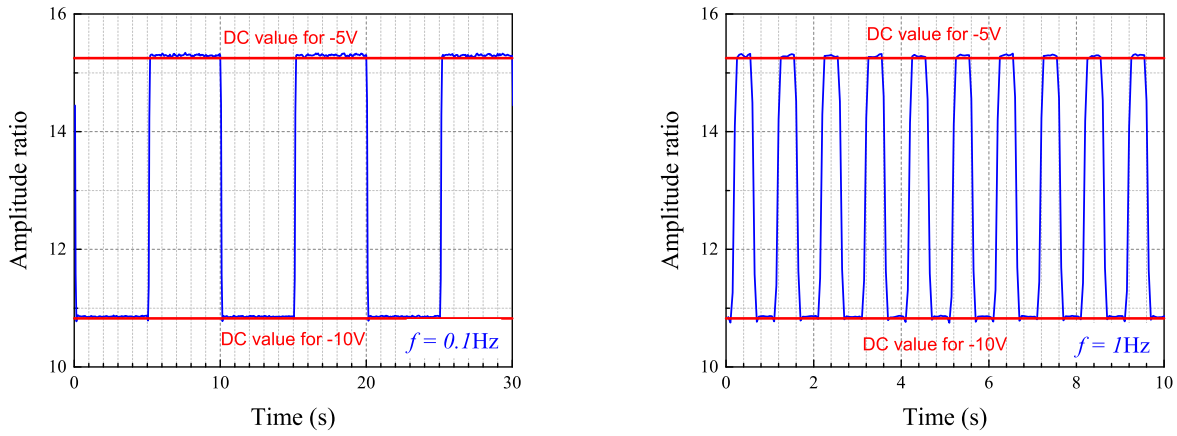

(a) (b)

Fig. 13. Real-time monitoring of the amplitude ratio for different input perturbation frequencies, f: (a) $f = 0.1$Hz and (b) $f = 1$Hz. The input perturbation voltage was switched between -5V and -10V. The DC values of amplitude ratio for those particular perturbation voltages are shown in red.

is being studied. This work initializes the optimization that can be done by tuning the operating region with respect to the coupling voltage, amplitude ratio and non-linear vibrations. Future work on this will entail deriving the theory for optimizing the noise in mode localized resonators with dominating thermo-mechanical noise and validating it using experiments and simulations.

APPENDIX A
DERIVATION OF TRANSFER FUNCTIONS

The equations of motion of the two resonator system can be expressed as follows:

$$M_1\ddot{X}_1 + c_1\dot{X}_1 + K_1X_1 + K_c(X_1 - X_2) = F_1 \quad (21a)$$

$$M_2\ddot{X}_2 + c_2\dot{X}_2 + K_2X_2 + K_c(X_2 - X_1) = F_2 \quad (21b)$$

In the laplace domain, these equations are expressed as:

$$M_1s^2X_1(s) + c_1sX_1(s) + (K_1 + K_c)X_1(s) = F_1 + K_cX_2(s) \quad (22a)$$

$$M_2s^2X_2(s) + c_2sX_2(s) + (K_2 + K_c)X_2(s) = F_2 + K_cX_1(s) \quad (22b)$$

This can be simplified to

$$H_1(s)X_1(s) = F_1(s) + K_cX_2(s) \quad (23a)$$

$$H_2(s)X_2(s) = F_2(s) + K_cX_1(s) \quad (23b)$$

where

$$H_1(s) = M_1s^2 + c_1s + (K_1 + K_c) \quad (24a)$$

$$H_2(s) = M_2s^2 + c_2s + (K_2 + K_c) \quad (24b)$$

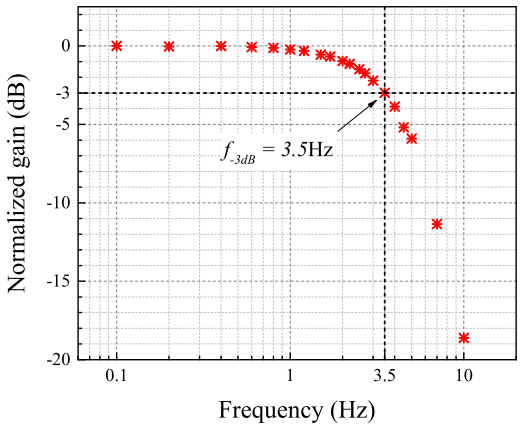

Fig. 14. Measured sensitivity, normalized to DC sensitivity, with respect to the frequency of perturbation. It can be seen that the 3dB bandwidth of the sensor system under test is 3.5Hz.

Using Cramer's rule, the displacement of each resonator in response to each one of the forces can be derived as follows:

$$\begin{bmatrix} H_1(s) & -K_c \\ -K_c & H_2(s) \end{bmatrix} \begin{bmatrix} X_1 \\ X_2 \end{bmatrix} = \begin{bmatrix} F_1 \\ F_2 \end{bmatrix} \tag{25}$$

$$X1 = \frac{\begin{vmatrix} F_1 & -K_c \\ F_2 & H_2(s) \end{vmatrix}}{\begin{vmatrix} H_1(s) & -K_c \\ -K_c & H_2(s) \end{vmatrix}}; X2 = \frac{\begin{vmatrix} H_1(s) & F1 \\ -K_c & F2 \end{vmatrix}}{\begin{vmatrix} H_1(s) & -K_c \\ -K_c & H_2(s) \end{vmatrix}}; \tag{26}$$

$$X_1 = \frac{F_1 H_2(s) + K_c F_2}{H_1(s)H_2(s) - K_c^2}; X_2 = \frac{F_2 H_1(s) + K_c F_1}{H_1(s)H_2(s) - K_c^2}; \tag{27}$$

Using Eq. 27, the transfer function of the displacement of resonator *i* due to force on the *j*th resonator can be described as

$$X_i = \sum_{j=1}^{2} H_{ij} F_j \tag{28}$$

where transfer functions (H_{ij}) for various inputs and outputs can be described as follows:

$$\begin{aligned} H_{11} &= \frac{H_2(s)}{H_1(s)H_2(s) - K_c^2}; H_{12} = \frac{K_c}{H_1(s)H_2(s) - K_c^2}; \\ H_{21} &= \frac{K_c}{H_1(s)H_2(s) - K_c^2}; H_{22} = \frac{H_1(s)}{H_1(s)H_2(s) - K_c^2}; \end{aligned} \tag{29}$$

ACKNOWLEDGMENT

The authors would like to acknowledge the funding from Innovate UK and the Natural Environment Research Council.

REFERENCES

[1] M. Pandit, C. Zhao, G. Sobreviela, A. Mustafazade, and A. A. Seshia, "Closed-loop tracking of amplitude and frequency in a mode-localized resonant mems sensor," in *International Frequency Control Symposium (IFCS), 2017 IEEE 71st*. IEEE, 2017.

[2] R. N. Candler, M. A. Hopcroft, B. Kim, W.-T. Park, R. Melamud, M. Agarwal, G. Yama, A. Partridge, M. Lutz, and T. W. Kenny, "Long-term and accelerated life testing of a novel single-wafer vacuum encapsulation for mems resonators," *Journal of Microelectromechanical Systems*, vol. 15, no. 6, pp. 1446–1456, 2006.

[3] B. Kim, R. N. Candler, M. A. Hopcroft, M. Agarwal, W.-T. Park, and T. W. Kenny, "Frequency stability of wafer-scale film encapsulated silicon based mems resonators," *Sensors and Actuators A: Physical*, vol. 136, no. 1, pp. 125–131, 2007.

[4] Y. Chen, D. D. Shin, I. B. Flader, and T. W. Kenny, "Tri-mode operation of highly doped silicon resonators for temperature compensated timing references," in *Micro Electro Mechanical Systems (MEMS), 2017 IEEE 30th International Conference on*. IEEE, 2017, pp. 1158–1161.

[5] C. T.-C. Nguyen, "Mems technology for timing and frequency control," *IEEE transactions on ultrasonics, ferroelectrics, and frequency control*, vol. 54, no. 2, 2007.

[6] S. Gong and G. Piazza, "Design and analysis of lithium–niobate-based high electromechanical coupling rf-mems resonators for wideband filtering," *IEEE Transactions on Microwave Theory and Techniques*, vol. 61, no. 1, pp. 403–414, 2013.

[7] X. Zou, P. Thiruvenkatanathan, and A. A. Seshia, "A seismic-grade resonant mems accelerometer," *Journal of Microelectromechanical Systems*, vol. 23, no. 4, pp. 768–770, 2014.

[8] G. Langfelder, A. Caspani, and A. Tocchio, "Design criteria of low-power oscillators for consumer-grade mems resonant sensors," *IEEE Transactions on Industrial Electronics*, vol. 61, no. 1, pp. 567–574, 2014.

[9] S. A. Zotov, B. R. Simon, A. A. Trusov, and A. M. Shkel, "High quality factor resonant mems accelerometer with continuous thermal compensation," *IEEE Sensors Journal*, vol. 15, no. 9, pp. 5045–5052, 2015.

[10] Y. Wang, H. Ding, X. Le, W. Wang, and J. Xie, "A mems piezoelectric in-plane resonant accelerometer based on aluminum nitride with two-stage microleverage mechanism," *Sensors and Actuators A: Physical*, vol. 254, pp. 126–133, 2017.

[11] M. Li, E. Ng, V. Hong, C. Ahn, Y. Yang, T. Kenny, and D. Horsley, "Lorentz force magnetometer using a micromechanical oscillator," *Applied Physics Letters*, vol. 103, no. 17, p. 173504, 2013.

[12] Y. Hui, T. Nan, N. X. Sun, and M. Rinaldi, "High resolution magnetometer based on a high frequency magnetoelectric mems-cmos oscillator," *Journal of Microelectromechanical Systems*, vol. 24, no. 1, pp. 134–143, 2015.

[13] J. L. Fu, R. Tabrizian, and F. Ayazi, "Dual-mode aln-on-silicon micromechanical resonators for temperature sensing," *IEEE Transactions on Electron Devices*, vol. 61, no. 2, pp. 591–597, 2014.

[14] R. Tabrizian and F. Ayazi, "Dual-mode vertical membrane resonant pressure sensor," in *Micro Electro Mechanical Systems (MEMS), 2014 IEEE 27th International Conference on*. IEEE, 2014, pp. 120–123.

[15] E. Rubiola, *Phase noise and frequency stability in oscillators*. Cambridge University Press, 2008.

[16] J. C. Salvia, R. Melamud, S. A. Chandorkar, S. F. Lord, and T. W. Kenny, "Real-time temperature compensation of mems oscillators using an integrated micro-oven and a phase-locked loop," *Journal of Microelectromechanical Systems*, vol. 19, no. 1, pp. 192–201, 2010.

[17] I. P. Prikhodko, A. A. Trusov, and A. M. Shkel, "Compensation of drifts in high-q mems gyroscopes using temperature self-sensing," *Sensors and Actuators A: Physical*, vol. 201, pp. 517–524, 2013.

[18] R. H. OlssonIII, K. E. Wojciechowski, M. S. Baker, M. R. Tuck, and J. G. Fleming, "Post-cmos-compatible aluminum nitride resonant mems accelerometers," *Journal of Microelectromechanical Systems*, vol. 18, no. 3, pp. 671–678, 2009.

[19] A. Tocchio, A. Caspani, and G. Langfelder, "Mechanical and electronic amplitude-limiting techniques in a mems resonant accelerometer," *IEEE Sensors Journal*, vol. 12, no. 6, pp. 1719–1725, 2012.

[20] S. Seok, S. Seong, B. Lee, J. Kim, and K. Chun, "A high performance mixed micromachined differential resonant accelerometer," in *Sensors, 2002. Proceedings of IEEE*, vol. 2. IEEE, 2002, pp. 1058–1063.

[21] M. Spletzer, A. Raman, A. Q. Wu, X. Xu, and R. Reifenberger, "Ultrasensitive mass sensing using mode localization in coupled microcantilevers," *Applied Physics Letters*, vol. 88, no. 25, p. 254102, 2006.

[22] P. Thiruvenkatanathan, J. Yan, J. Woodhouse, and A. A. Seshia, "Enhancing parametric sensitivity in electrically coupled mems resonators," *Journal of Microelectromechanical Systems*, vol. 18, no. 5, pp. 1077–1086, 2009.
[23] P. Thiruvenkatanathan, J. Yan, and A. A. Seshia, "Differential amplification of structural perturbations in weakly coupled mems resonators," *IEEE transactions on ultrasonics, ferroelectrics, and frequency control*, vol. 57, no. 3, pp. 690–697, 2010.
[24] H. Zhang, J. Zhong, W. Yuan, J. Yang, and H. Chang, "Ambient pressure drift rejection of mode-localized resonant sensors," in *2017 IEEE 30th International Conference on Micro Electro Mechanical Systems (MEMS)*. IEEE, 2017, pp. 1095–1098.
[25] P. W. Anderson, "Absence of diffusion in certain random lattices," *Physical review*, vol. 109, no. 5, p. 1492, 1958.
[26] C. Zhao, G. S. Wood, J. Xie, H. Chang, S. H. Pu, and M. Kraft, "A comparative study of output metrics for an mems resonant sensor consisting of three weakly coupled resonators," *Journal of Microelectromechanical Systems*, vol. 25, no. 4, pp. 626–636, 2016.
[27] H. Zhang, B. Li, W. Yuan, M. Kraft, and H. Chang, "An acceleration sensing method based on the mode localization of weakly coupled resonators," *Journal of Microelectromechanical Systems*, vol. 25, no. 2, pp. 286–296, 2016.
[28] P. Thiruvenkatanathan and A. Seshia, "Mode-localized displacement sensing," *Journal of Microelectromechanical Systems*, vol. 21, no. 5, pp. 1016–1018, 2012.
[29] H. Zhang, J. Huang, W. Yuan, and H. Chang, "A high-sensitivity micromechanical electrometer based on mode localization of two degree-of-freedom weakly coupled resonators," *Journal of Microelectromechanical Systems*, vol. 25, no. 5, pp. 937–946, 2016.
[30] G. S. Wood, C. Zhao, S. H. Pu, S. A. Boden, I. Sari, and M. Kraft, "Mass sensor utilising the mode-localisation effect in an electrostatically-coupled mems resonator pair fabricated using an soi process," *Microelectronic Engineering*, vol. 159, pp. 169–173, 2016.
[31] C. Zhao, M. H. Montaseri, G. S. Wood, S. H. Pu, A. A. Seshia, and M. Kraft, "A review on coupled mems resonators for sensing applications utilizing mode localization," *Sensors and Actuators A: Physical*, vol. 249, pp. 93–111, 2016.
[32] C. Zhao, G. S. Wood, J. Xie, H. Chang, S. H. Pu, and M. Kraft, "A force sensor based on three weakly coupled resonators with ultrahigh sensitivity," *Sensors and Actuators A: Physical*, vol. 232, pp. 151–162, 2015.
[33] C. Zhao, M. Pandit, B. Sun, G. Sobreviela, X. Zou, and A. Seshia, "A closed-loop readout configuration for mode-localized resonant mems sensors," *Journal of Microelectromechanical Systems*, vol. 26, no. 3, pp. 501–503, 2017.
[34] P. Thiruvenkatanathan, J. Woodhouse, J. Yan, and A. A. Seshia, "Limits to mode-localized sensing using micro- and nanomechanical resonator arrays," *Journal of Applied Physics*, vol. 109, no. 10, p. 104903, 2011.
[35] P. Saulson, "Thermal noise in mechanical experiments," *Physical Review D*, vol. 42, pp. 2437–2445, 1990.
[36] G. Ferrari, F. Gozzini, A. Molari, and M. Sampietro, "Transimpedance amplifier for high sensitivity current measurements on nanodevices," *IEEE Journal of Solid-State Circuits*, vol. 44, no. 5, pp. 1609–1616, 2009.
[37] G. Ferrari and M. Sampietro, "Wide bandwidth transimpedance amplifier for extremely high sensitivity continuous measurements," *Review of scientific instruments*, vol. 78, no. 9, p. 094703, 2007.
[38] R. C. Elandt-Johnson and N. L. Johnson, *Survival Models and Data Analysis*. John Wiley and Sons, 1980.
[39] A. Stuart and K. Ord, *Kendall's Advanced Theory of Statistics, Distribution Theory*, 6th ed. Arnold, 1994, vol. 1.

Milind Pandit received his BASc degree in electrical and electronics engineering with a specialization in Micro and Nano technology from the University of British Columbia, Vancouver, British Columbia, Canada. He is currently pursuing his Ph.D. degree in the MEMS research group at the Nanoscience Centre, Dept. of Engineering at the University of Cambridge, Cambridge, UK. His current research interests include micro-electromechanical systems (MEMS) and inertial sensors design with emphasize on coupled resonators topology.

Chun Zhao received the B.Eng. degree in measurement and control technology and instrument from the Huazhong University of Science and Technology, Wuhan, China, in 2009; the M.Sc. degree in analog and digital IC design from Imperial College London, London, U.K., in 2011; and the Ph.D. degree in microelectromechanical systems (MEMS) from the University of Southampton, Southampton, U.K., in 2016.

From April 2015 to March 2016, he was a full time Research Scientist at Sharp Laboratories of Europe, Oxford, U.K., working on the research and development of acoustic MEMS devices and integrated control circuit design. He joined the Department of Engineering, University of Cambridge in April 2016, where he is currently a Research Associate in MEMS. His current research interests include MEMS, microresonators, miniature sensors (such as inertial sensors) and actuators, MEMS system modelling and interface circuit for sensors design.

Guillermo Sobreviela was born in Huesca, Spain, in 1989. He received the bachelors degree in physics from the University of Zaragoza, Zaragoza, Spain, in 2012, and the masters degree in micro and nanoelectronics engineering and the Ph.D. degree in electronics from the Universitat Autnoma de Barcelona, Barcelona, Spain, in 2013 and 2016, respectively. Currently is a Research Associate in Microsystems (MEMS) at the Cambridge University.

His current research interests include RF coupled MEMS resonators and the integration of RF MEMS into CMOS technologies, focusing on the design of monolithic CMOS-MEMS oscillators for time reference and resonance tracking based sensors.

Arif Mustafazade (Aref Mostafazadeh) was born in 1978 in Tabriz, Iran. He received his B.S. degree in Electrical and Electronics Engineering from Tabriz Azad University (TAU), Tabriz, Iran in 2001, his M.A. degree in Photography from the Fine Arts Department of Marmara University, Istanbul, Turkey in 2008, his M.S. degree in Electrical and Computer Engineering and Ph.D. degree in Electrical and Electronics Engineering from Ko University (KU), Istanbul, Turkey in 2010 and 2016, respectively. He is currently pursuing his research on MEMS resonant gravity sensors at the University of Cambridge.

Arif started learning electronics from the age of eight as a hobby and worked as a designer for a private research firm in Tabriz during his high-school and university years in Iran. In 2006, he moved to Istanbul to enroll in the MA program in Photography of Marmara University where he worked on the imaging optics and quality factors of imaging systems. He worked as a research and teaching assistant in the KU Laser Research Lab from 2008 to 2010 and in the KU Optical Microsystems Lab from 2010 to 2015. In 2015, he founded the Electronics Research Lab in GAMAK Motors Company, the largest electric motor manufacturer in Turkey and started as chief design engineer and research scientist. In 2016, he moved to United Kingdom and started to work in the University of Cambridge.

His research interests also include lasers and optics, optical MEMS sensors, resonance tracking systems, Phase-Locked Loops, metrology, high-precision measurement and control systems, thermal design and power electronics.

Sijun Du (S14) received the B.Eng. degree in electrical engineering from University Pierre and Marie Curie, Paris, France, in 2011, and the M.Sc. degree in electrical and electronics engineering from Imperial College, London, U.K., in 2012. He is currently pursuing the Ph.D. degree with the University of Cambridge, Cambridge, U.K.

He was with the Laboratory LIP6, University Pierre and Marie Curie, Paris; and then, a Digital IC Engineer in Shanghai from 2012 to 2014. He is currently with the Cambridge Nanoscience Centre, University of Cambridge. His current research interests include macroscopic and microelectromechanical systems energy harvesters, associated interface circuits, power electronics, power management circuits, dcdc converters, and rectification circuits.

Xudong Zou received the B.Sc. degree in microelectronics from Peking University, China, in 2009, and the Ph.D. degree in mechanics, materials and design from the University of Cambridge, U.K., in 2013. He was afliated with the Nanoscience Center, Department of Engineering, University of Cambridge, as a Research Associate, and the Churchill College as a Post-Doctoral By-Fellow.

He is currently a Professor with the State Key Laboratory of Transducer Technology, Institute of Electronics, Chinese Academy of Sciences. His main research interest lies in the area of integrated micro and nano electromechanical systems, with a focus on resonators and inertial sensors, including design and optimization of high resolution MEMS resonant inertial sensors, studying the nonlinear effects on the noise processes in MEMS oscillators, and the coupled MEMS resonators in sensing and signal processing applications.

Ashwin Seshia received his BTech in Engineering Physics in 1996 from IIT Bombay, MS and PhD degrees in Electrical Engineering and Computer Sciences from the University of California, Berkeley in 1999 and 2002 respectively, and the MA from the University of Cambridge in 2008. During his time at the University of California, Berkeley, he was affiliated with the Berkeley Sensor & Actuator Center. He joined the faculty of the Engineering Department at the University of Cambridge in October 2002 where he is presently a Professor in Microsystems Technology and a Fellow of Queens' College. He is a Fellow of the Institute of Physics, a Fellow of the Institution for Engineering and Technology and a senior member of the Institute of Electrical and Electronics Engineers. His research interests are in the domain of microengineered dynamical systems with applications to sensors and sensor systems. Dr Seshia serves on the editorial boards of the IEEE Journal of Microelectromechanical systems, the IOP Journal of Micromechanics and Microengineering, the IEEE Transactions on Nanotechnology and the IEEE Transactions on Ultrasonics, Ferroelectrics and Frequency Control.